

# Intrinsic Dimensionality of Fermi-Pasta-Ulam-Tsingou High-Dimensional Trajectories Through Manifold Learning

Gionni Marchetti <sup>\*</sup>  
(Dated: November 5, 2024)

A data-driven approach based on unsupervised machine learning is proposed to infer the intrinsic dimensions  $m^*$  of the high-dimensional trajectories of the Fermi-Pasta-Ulam-Tsingou (FPUT) model. Principal component analysis (PCA) is applied to trajectory data consisting of  $n_s = 4,000,000$  datapoints, of the FPUT  $\beta$  model with  $N = 32$  coupled oscillators, revealing a critical relationship between  $m^*$  and the model's nonlinear strength. For weak nonlinearities,  $m^* \ll n$ , where  $n = 2N$ . In contrast, for strong nonlinearities,  $m^* \rightarrow n - 1$ , consistently with the ergodic hypothesis. Furthermore, one of the potential limitations of PCA is addressed through an analysis with t-distributed stochastic neighbor embedding (*t*-SNE). Accordingly, we found strong evidence suggesting that the datapoints lie near or on a curved low-dimensional manifold for weak nonlinearities.

## I. INTRODUCTION

The Fermi-Pasta-Ulam-Tsingou (FPUT) model was primarily conceived to test the validity of the equipartition theorem, a fundamental result of classical statistical mechanics, through computer simulations of its nonlinear dynamics [1–4]. Fermi who “foresaw the dawning of computational science” [5], expected that the simulations of the dynamics of a one-dimensional set of weakly coupled harmonic oscillators obtained through MANIAC-I computer [6, 7], would support the equipartition theorem, and hence confirm Boltzmann’s *ergodic hypothesis* [8–10] [11]. The ergodic hypothesis is commonly assumed to hold when carrying out the molecular dynamics simulations [12], even though many systems, such as glasses and nearly harmonic solids, are not ergodic in principle [13]. Nevertheless, the recurrences observed in simulations of coupled harmonic oscillators, first performed by Mary Tsingou, appeared to challenge this assumption [1, 2, 14]. This surprising result, known as the FPUT paradox, prompted numerous efforts to understand the system’s dynamics through both numerical and theoretical investigations, leading to several important findings [15–19]. In this regard, it is worth recalling here that the Kolmogorov-Arnol’d-Moser (KAM) theorem was proposed as a plausible explanation of its quasi-periodic behavior [20, 21]. According to the KAM theory, one would expect that at low energy densities or for small nonlinearities, the trajectories are subject to a periodic motion on invariant tori embedded in the phase space of dimension  $n$  ( $n = 2N$ , where  $N$  is the number of oscillators) [21–23].

On the other hand, the state of the FPUT system can be considered a point in the phase space as typically assumed within the microcanonical formalism of statistical mechanics [24]. As a result, during the system’s time-evolution, such a point traces out a trajectory that always stays on the hypersurface of constant energy  $\Sigma_E = \{(q, p) : H(q, p) = E\}$ , where  $H$  and  $q, p$  denote

the system’s Hamiltonian and the canonical coordinates, respectively. Accordingly,  $\Sigma_E$  has dimension  $n - 1$ , but the KAM invariant tori have dimensions  $N$ . The previous observation suggests there must exist a critical relationship between the intrinsic (or effective) dimension of the phase points belonging to the FPUT’s high-dimensional trajectories and the model’s non-linear strength, the latter depending on the model’s parameters  $\alpha$  and  $\beta$  and on the system’s energy density (see Sec. II for details).

In this paper, we aim to unravel such a relationship by investigating the intrinsic dimension of the phase points belonging to trajectories of the FPUT  $\beta$  model, where  $\alpha = 0$  and  $N = 32$ , using a data-driven approach based on the principal component analysis (PCA), a workhorse in the unsupervised machine learning (ML) and statistics [25–27]. PCA is a simple and computationally efficient linear dimensionality reduction technique (linear encoder), that identifies the best-fitting  $m$ -dimensional linear subspace  $U \subset \mathbb{R}^n$  for a given data set consisting of  $n_s$  datapoints by minimizing the reconstruction error  $J_m$ . In the following, the reconstruction errors will be computed for datasets, each of which is formed by an entire large trajectory ( $n_s = 4,000,000$ )—thus avoiding random sampling—accurately generated through the Verlet integration [28, 29], starting from the initial condition corresponding to initially exciting either first ( $k = 1$ ) or second ( $k = 2$ ) mode (see Sec. II for details). Subsequently, each value  $m^*$  of the searched intrinsic dimension will be inferred from the respective reconstruction error curve. Accordingly, our dimensionality reduction approach predicts that  $m^*$  monotonically increases with the nonlinear-strength parameter  $\beta$  (see Fig. 4 and Fig. 7). In the case of  $k = 1$ , two sharply separated asymptotic regions of low ( $m^* \ll n$ ) and high dimensionality ( $m^* \rightarrow n - 1$ ), approximately located at  $\beta \lesssim 1$  (weak nonlinearity) and  $\beta \gtrsim 2$  (strong nonlinearity), respectively, stem from this monotonic dependence. Remarkably, these regions occur in correspondence with the two main dynamical features of the  $\beta$  model with  $N = 32$ : the recurrences observed when  $\beta \lesssim 1$  (see Fig. 1) and the mixing for which the initially excited first mode starts to share its energy efficiently when  $\beta \rightarrow 3$  (see Fig. 2). However, in the case of  $k = 2$ , where much stronger nonlinearities are present,

<sup>\*</sup> [gionnimarchetti@gmail.com](mailto:gionnimarchetti@gmail.com)

trajectories with significantly higher intrinsic dimensions emerge even at small  $\beta$  values. This aligns with the ergodic hypothesis, as one would expect the phase points to lie near or on  $\Sigma_E$  when the mixing occurs due to the strong nonlinear dynamics.

However, in the present work, we could only estimate the intrinsic dimensions crudely for two reasons. First, the standard method for determining  $m^*$  from the error reconstruction curves relies on detecting an elbow (or equivalently a knee) [30, 31], which is not easily identifiable for this problem. Therefore, we resorted to an alternative approach that involved introducing a reasonably small threshold,  $J_m^{\text{th}}$  for the reconstruction error. In this approach,  $m^*$  is defined as the minimum value of  $m$  for which  $J_m \lesssim J_m^{\text{th}}$  (see Sec. IV for details). Second, but more importantly, PCA presents some serious limitations. First, it fails to uncover nonlinear structures present in the data under analysis [30, 32, 33]. Second, PCA cannot handle data with higher-order dependencies and tends to preserve large pairwise distances between datapoints [34]. The latter implies that it may miss interesting structures characterized by smaller distances [35].

To address the first potential issue due to nonlinearity in the simulation data exhibiting the energy recurrences ( $k = 1$ ), we employ  $t$ -distributed stochastic neighbor embedding ( $t$ -SNE), an unsupervised non-parametric algorithm [36] that preserves both local and global structures of the high-dimensional data, once the PCA initialization is provided [37–40]. By visualizing the  $t$ -SNE embeddings in two dimensions, we found strong evidence suggesting that the datapoints lie near or on a curved low-dimensional manifold when  $\beta \lesssim 1$ . This important result suggests that other nonlinear machine learning methods, e.g., neural network architectures like autoencoders [32, 33, 41, 42], should complement our current approach. However, we do not anticipate that these methods will alter the overall picture reasonably provided by PCA; rather, they are expected to yield more accurate estimates of  $m^*$ . We will discuss how to possibly overcome the above PCA limitations and the potential directions for future research in Sec. V.

## II. THE FERMI-PASTA-ULAM-TSINGOU MODEL

The original Fermi-Pasta-Ulam-Tsingou model describes a one-dimensional system of  $N$  coupled harmonic oscillators whose Hamiltonian  $H(q, p)$  where  $q = (q_0, q_1, \dots, q_N)$  and  $p = (p_0, p_1, \dots, p_N)$ , reads [1]

$$H(q, p) = \frac{1}{2} \sum_{i=1}^N p_i^2 + \frac{1}{2} \sum_{i=0}^N (q_{i+1} - q_i)^2 + \frac{\alpha}{3} \sum_{i=0}^N (q_{i+1} - q_i)^3 + \frac{\beta}{4} \sum_{i=0}^N (q_{i+1} - q_i)^4. \quad (1)$$

The nonlinearity of such a model chiefly arises from the parameters  $\alpha$  and  $\beta$ . But, it can be shown using scaling arguments that the quantities  $\alpha\sqrt{\epsilon}$  and  $\beta\epsilon$  determine the degree of nonlinearity [43, 44]. Here  $\epsilon$  denotes the energy per particle (or energy density), that is,  $\epsilon = E/N$ ,  $E$  being the total energy.

By means of the normal mode coordinates  $a_k$  ( $k = 1, 2, \dots, N$ ) [2, 45] for which

$$a_k = \sqrt{\frac{2}{N+1}} \sum_{j=0}^N q_j \sin\left(\frac{jk\pi}{N+1}\right), \quad (2)$$

and neglecting the terms arising from the cubic and quartic terms in the Hamiltonian [46], one can express the energy  $E_k$  of normal  $k$ -th mode as [1, 45]

$$E_k = \frac{1}{2} [\dot{a}_k^2 + \omega_k^2 a_k^2]. \quad (3)$$

where  $\omega_k = 2 \sin(k\pi/2(N+1))$  is the frequency of the normal  $k$ -th mode. We note in passing that one can assume in good approximation that for weak nonlinearity  $E = \sum_{i=1}^N E_k$  [47].

In the following, we shall limit ourselves to the  $\beta$ -model, where  $\alpha = 0$ , that corresponds to a perturbation of strength  $\beta$  ( $\beta > 0$ ) of the linear chain of oscillators due to the quartic potential, i.e., the fourth term of Eq. 1. Furthermore, we shall study the  $\beta$ -model dynamics assuming fixed boundary conditions, i.e.,  $q_0 = q_{N+1} = 0$ .

The typical initial conditions at time  $t = 0$  are given as by the following formula [2, 45]

$$q_i(0) = A \sqrt{\frac{2}{N+1}} \sin\left(\frac{ik\pi}{N+1}\right), \quad (4)$$

where  $A$  denotes the amplitude. In the following, we shall set  $A = 10$  [45]. The initial conditions under scrutiny correspond to the first mode (i.e.,  $k = 1$ ) or the second mode (i.e.,  $k = 2$ ) being initially excited, as shown in Fig. 9.

We chose the velocity Verlet algorithm [28] for integrating the FPUT model's canonical equations of motion, dictated by the Hamiltonian (Eq. 1) [48]. Such an algorithm is symplectic as required for the problem at hand [29, 49], and also a second-order method with local and global integration errors that scale as  $\mathcal{O}(h^4)$  and  $\mathcal{O}(h^2)$ , respectively,  $h$  being the finite-sized time step [50].

We tested our numerical simulations against those reported in Ref. [45], for which it was assumed  $h = 0.05$ , finding an excellent agreement between them.

In Fig. 1 we plot the energies  $E_k$  for the normal modes  $k = 1, 3, 5$  as functions of time  $t$  in units of recurrence time  $t_r = 2 \times 10^5$  [46], assuming  $\beta = 0.3$  and  $N = 32$ . The initial condition corresponds to initially giving the energy  $\mathcal{E}_1$  ( $\mathcal{E}_1 \approx 0.45$ ) to the first normal mode. The time-dependence of these energies  $E_k$  illustrates the typical observed recurrence phenomenon occurring for small nonlinearities [14]. It is also worth noting that in such a case there cannot be energy sharing with even modes, that is,

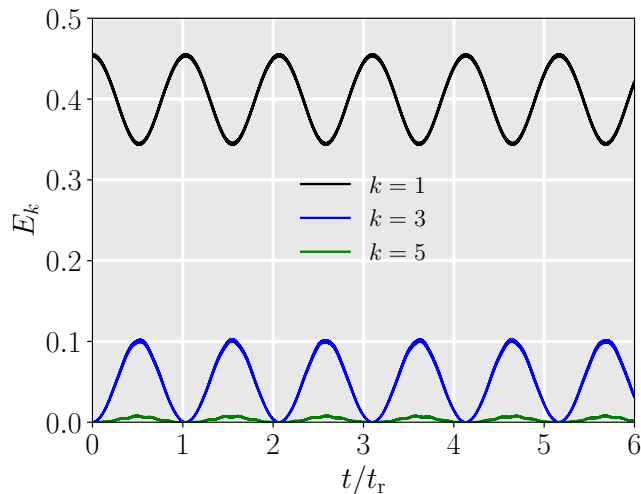


FIG. 1. The energy  $E_k$  of modes for  $k = 1, 3, 5$  as a function of time  $t$  in units of recurrence time  $t_r$  ( $t_r = 2 \times 10^5$ ) for  $\beta$  model with  $\beta = 0.3$ , assuming  $N = 32$ . The system's equations of motion were numerically integrated with time step  $h = 0.05$ . The initial condition is set to provide the energy  $\mathcal{E} \approx 0.45$  to the first normal mode ( $k = 1, A = 10$ ).

modes whose wave number  $k$  is equal to an even number. This is due to the symmetric nature of the  $\beta$ -model [46, 47]. On the other hand, for strong non-linearities, the first mode efficiently shares its energy with the different modes, including the even modes (violation of “parity conservation”) as shown for the modes  $k = 1, 2, 3, 4$ , in Fig. 2, assuming  $\beta = 3$ . This behavior leads to an irreversible energy mixing. In the following, we will refer to this regime simply as “mixing” for brevity.

### III. METHODOLOGY

In the following, we shall briefly recall the main results of the unsupervised ML algorithms we employed for the dimensional reduction of the data generated from the high-dimensional FPUT trajectories. We leveraged the principal component analysis to compute the reconstruction error  $J_m$  of the original data's orthogonal projections onto a suitable linear subspace  $U \subset \mathbb{R}^n$  of dimension  $m$ , while  $t$ -SNE helped us visualize in two-dimensions the embedding arising from a given trajectory in the early stage of the system's dynamics.

In the present work, a trajectory, including its initial condition, forms a data set  $\mathcal{X} = \{x_1, x_2, \dots, x_{n_s}\}$ , where each element  $x_i$ , is a point in the phase space  $\mathbb{R}^n$ . Accordingly, each phase point represents the system's position along the orbit as time  $t$  increases monotonically from zero. A  $n_s \times n$  data matrix  $X$  can be constructed by setting each  $x_i$  as a row of  $X$ , where  $i$  runs from 1 to  $n_s$ .

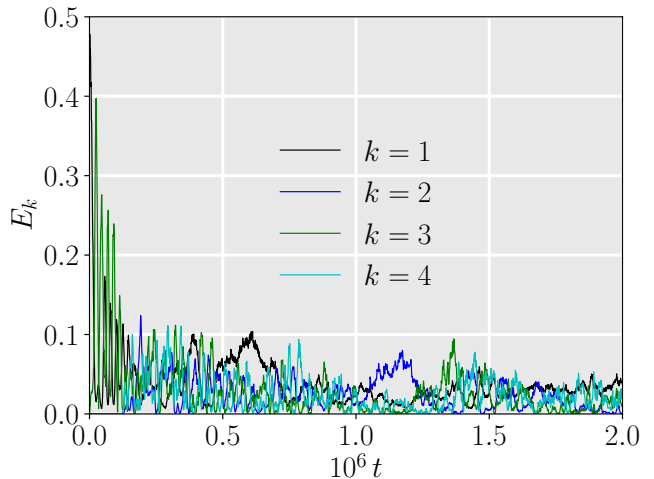


FIG. 2. The energy of modes  $E_k$  for  $k = 1, 2, 3, 4$  as a function of time  $t$  for  $\beta$  model with  $\beta = 3$ , assuming  $N = 32$ . The system's equations of motion were numerically integrated with time step  $h = 0.05$ . The initial condition is set to provide the energy  $\mathcal{E} \approx 0.45$  to the first normal mode ( $k = 1, A = 10$ ).

#### A. PCA and the Reconstruction Error

Principal component analysis can be understood as a dimensionality reduction method that either maximally preserves the overall variance of the original high-dimensional data along the principal components [26, 34, 51, 52] or orthogonally projects the data onto suitable lower-dimensional linear subspace  $U$ , commonly known as principal subspace, of dimension  $m$ , minimizing the average reconstruction error  $J_m$ . Basically, starting with the data-points  $x_i$  with  $i = 1, \dots, n_s$  in  $\mathbb{R}^n$ , then reconstruction error  $J_m$  for approximating each  $x_i$  by its orthogonal projection  $\tilde{x}_i \in U$ , is the average squared Euclidean distance defined as follows [25, 27]

$$J_m = \frac{1}{n_s} \sum_{j=1}^{n_s} \|x_j - \tilde{x}_j\|^2, \quad (5)$$

where the symbol  $\| \cdot \|$  denotes the Euclidean norm. According to PCA, such an error can be computed through the explained variance  $\lambda_i$ , corresponding to the  $i$ -th principal component (PC), and reads [27]

$$J_m = \sum_{l=m+1}^n \lambda_l. \quad (6)$$

The explained variances  $\lambda_l$  with  $l = 1, \dots, n$  are the eigenvalues of the (sample) covariance matrix  $S = \frac{1}{n_s-1} X^T X$ , where  $X^T$  denotes the transpose of data matrix  $X$  [26]. In Eq. 6 it is assumed that the eigenvalues are the smallest, that is,  $\lambda_1, \dots, \lambda_m$  are the largest in descending order [27]. Note that the eigenvectors relative

to the eigenvalues  $\lambda_l$  with  $l \geq m + 1$  constitute the basis of the orthogonal complement of the principal subspace  $U$ .

In the following, the eigenvalues  $\lambda_i$  will be efficiently computed via singular value decomposition (SVD) applied to matrix  $\tilde{X}$ , obtained after centering  $X$ . Then, SVD yields  $\tilde{X} = WLV^T$  where  $W$  and  $V$  are two suitable orthogonal matrices, and  $L$  is a diagonal matrix [26, 53, 54] whose eigenvalues  $s_i$  are called the singular values of  $\tilde{X}$ . Accordingly, one finds that the following relationship between  $\lambda_i$  and  $s_i$  [34]:

$$\lambda_i = \frac{s_i^2}{(n_s - 1)}. \quad (7)$$

Note that in Eq. 7 it is assumed that  $s_1^2 \geq s_2^2 \geq \dots \geq s_n^2 \geq 0$ .

Note that we will center the data before performing the singular value decomposition through data standardization, as is customary in machine learning [26, 55, 56]. As a result, the sum of the eigenvalues  $\lambda_i$  equals  $n$ , i.e.,  $\sum_{j=1}^n \lambda_i = n$ .

## B. t-Distributed Stochastic Neighbor Embedding

The  $t$ -SNE finds a low-dimensional representation  $\mathcal{Y}$ , often called embedding or map, of the high-dimensional data set  $\mathcal{X}$ , by minimizing the Kullback-Leibler (KL) divergence between the joint probabilities (or pairwise similarities)  $p_{ij}$  in the high-dimensional space and the joint probabilities  $q_{ij}$  in low-dimensional space. The joint probability  $p_{ij}$  ( $p_{ij} = 0$  if  $i = j$ ) is defined as

$$p_{ij} = \frac{p_{j|i} + p_{i|j}}{2n_s}, \quad (8)$$

where  $p_{j|i}$  and  $p_{i|j}$  are conditional probabilities. For instance, the conditional probability that  $x_i$  would pick  $x_j$  as its neighbor is

$$p_{j|i} = \frac{\exp(-\|x_i - x_j\|^2/2\sigma_i^2)}{\sum_{k \neq i} \exp(-\|x_i - x_k\|^2/2\sigma_i^2)}, \quad (9)$$

where  $\sigma_i^2$  is the variance of the Gaussian kernel. The variance  $\sigma_i^2$  is determined by specifying the perplexity  $\mathcal{P}$  that takes its default values at 30 or 50 [39]. We note in passing that the parameter  $\mathcal{P}$  can be considered the effective number of neighbors [57].

In the low-dimensional space, the joint probabilities are  $q_{ij}$  ( $q_{ij} = 0$  if  $i = j$ ) are defined through the  $t$ -distribution with one degree of freedom (the Cauchy distribution). As a result, for any pair of map (or embedding) points  $y_i$  and  $y_j$ ,  $q_{ij}$  reads [38]

$$q_{ij} = \frac{\left(1 + \|y_i - y_j\|^2\right)^{-1}}{\sum_{k \neq l} \left(1 + \|y_k - y_l\|^2\right)^{-1}}. \quad (10)$$

The arrangement of the points in the low-dimensional space is finally achieved by minimizing the KL divergence  $\text{KL}(P||Q)$  (or loss function) that reads

$$\text{KL}(P||Q) = \sum_{ij} p_{ij} \log \frac{p_{ij}}{q_{ij}}. \quad (11)$$

We refer the reader to Ref. [39] for details about the optimization via gradient descent, and to Sec IV for the initialization and other computational information.

In the present work, we will also compute the conditional probabilities with the cosine similarity  $d_{\cos}$  for comparison with the results obtained using the Euclidean norm. The cosine similarity reads [27]

$$d_{\cos}(x_i, x_j) = \frac{x_i \cdot x_j}{\|x_i\| \|x_j\|}. \quad (12)$$

It is commonly believed that cosine distance is less affected by the *curse of dimensionality* compared to Euclidean distance, and it often performs better for high-dimensional data [58].

## IV. RESULTS AND DISCUSSION

In the following, we will apply PCA to datasets formed by the entire trajectories, each one generated for values of  $\beta$ , taken at the fixed step  $\Delta\beta = 0.1$  within the interval  $[0.1, 3]$  according to Ref. [45]. We assume the initial condition is equivalent to giving the energy  $\mathcal{E}_1 \approx 0.45$  to the first mode ( $k = 1, A = 10$ ). By leveraging large datasets of size  $n_s = 4,000,000$  that store all the information about the dynamics, we should prevent the reconstruction error  $J_m$  ( $m = 1, \dots, 63$ ) from being affected by any potential bias due to the specific sampling method. Note that the data will be standardized before performing PCA (data preprocessing) as typically done in machine learning [27][59]. In particular, centering the data guarantees that PCA will be efficiently performed via the singular value decomposition (see Sec. III A).

In Fig. 3, the reconstruction error  $J_m$  (in percentage) is shown as a function of the dimension  $m$  of the best-fitting linear subspace onto which the trajectory points  $x_i$  are orthogonally projected by minimizing  $J_m$ , for each value of  $\beta$  under scrutiny. The curves form two families determined by the non-linear strength  $\beta$ . One family emerges at small nonlinearities, i.e., when  $\beta \lesssim 1.0$ , whose curves fall off quickly, yielding very small intrinsic dimensions. The second family is formed by smoother curves that decrease gradually, starting from  $\beta \gtrsim 1.1$ . As a result, these curves yield larger intrinsic dimensions. We note that the origin of these different behaviors can be understood by examining the eigenvalues  $\lambda_i$ , contributing to Eq. 6. When  $\beta$  is small, only a few eigenvalues differ from zero significantly as shown in Fig. 14. For instance, when  $\beta = 0.1$ ,  $\lambda_1$  and  $\lambda_2$  account for most of the preserved variance. In this case, the sum of the first two principal components (PCs), PC1 and PC2, explains about 99% of

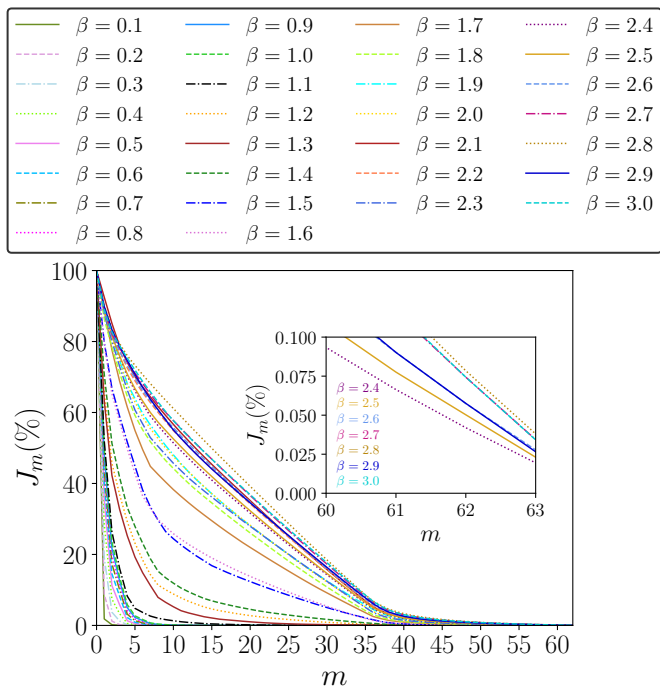


FIG. 3. Reconstruction error  $J_m$  in percentage (%) as a function of the dimension  $m$  of the best-fitting subspace  $U$  for  $\beta \in [0.1, 3]$ , using trajectories of  $N = 32$  coupled oscillators, consisting of  $n_s = 4,000,000$  datapoints, assuming the initial condition equivalent to giving the energy  $\mathcal{E}_1 \approx 0.45$  to the first mode ( $k = 1, A = 10$ ). Note that the zero of the horizontal axis is set at  $m = 1$ . (Inset) The same plot for  $m \in [60, 63]$  shows the curves corresponding to  $\beta \in [2.4, 3]$ .

the data variability as reported in Table I. Consequently, the curves in this family diminish quickly. In contrast, the curves of the other family originate from the contribution of a larger number of eigenvalues (approximately half of the total number when  $\beta \gtrsim 1.7$ ), making them smoother and more slowly decaying.

The standard method for estimating the intrinsic dimension  $m^*$  from a reconstruction error curve involves visually identifying the elbow (or equivalently the knee) of such a curve, beyond which  $J_m$  no longer decreases significantly as  $m$  increases [30]. However, the scrutinized curves do not exhibit sharp knees at strong nonlinearities. This typical issue makes the above method difficult to implement [60]. Furthermore, the curves decrease linearly as  $m$  increases (see the inset of Fig. 3), so  $J_m$  cannot be deemed constant anywhere. Therefore, we attempt to replace the overly subjective method described above with two alternative approaches. First, we shall automatically estimate  $m^*$  by identifying the elbow points, if these are *loosely defined* as points of maximum curvature, through the Kneedle algorithm, a general-purpose knee detection algorithm [31] [61]. However, this algorithm yields reasonable results only for very small values of  $\beta$ , but it proves valuable in illustrating the issues discussed above. Second, we shall introduce an arbitrarily small convenient

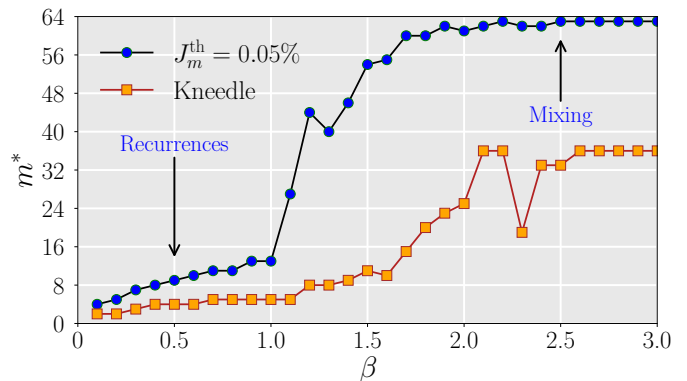


FIG. 4. The estimated intrinsic dimension  $m^*$  of entire trajectories ( $n_s = 4,000,000$ ) with system size  $N = 32$ , and the initial condition equivalent to giving the energy  $\mathcal{E}_1 \approx 0.45$  to the first normal mode ( $k = 1, A = 10$ ), as a function of  $\beta$ . The curves with circles and squares are computed assuming the threshold  $J_m^{\text{th}} = 0.05\%$  (circles) and using Kneedle (squares) with sensitivity  $s = 1$ , respectively.

threshold  $J_m^{\text{th}}$  for the reconstruction error, where  $m^*$  is the minimum value of  $m$  for which  $J_m \lesssim J_m^{\text{th}}$ . Accordingly, we set  $J_m^{\text{th}} = 0.05\%$ , based on the typical values of  $J_m$  (approximately  $0.02\% - 0.04\%$ ) reached when  $m = 63$  and  $\beta = 3$ . Such a convenient threshold ensures the existence of  $m^*$  across the entire range of  $\beta$  values.

In Fig. 4, the intrinsic dimension  $m^*$ , whose values are also displayed in Table I, as a function of  $\beta$  is shown. Its values are estimated by assuming  $J_m^{\text{th}} = 0.05$  (circles) and using Kneedle (squares). The algorithm is computed by setting the parameter  $s$ , called sensitivity, to unity. The sensitivity measures the number of flat points in the curve before declaring the knee [31]. In both cases,  $m^*$  increases monotonically with  $\beta$ . However, Kneedle yields reasonable dimensions only when  $\beta$  is very small, and in such a case the results align with those obtained using the threshold-based approach, but it fails to estimate  $m^*$  for most of the  $\beta$  values. We can understand this, by looking at how this algorithm works for two characteristic curves. In Fig. 5, where we set the zero of the horizontal axis at  $m = 1$  for better visualization, Kneedle ( $s = 1$ ) finds the elbow points at the intersection of two specific curves corresponding to  $\beta = 0.2$  and  $\beta = 2.6$ , with the vertical lines at  $m^* = 3$  (blue dashed line) and  $m^* = 37$  (black dashed line), respectively. For  $\beta = 0.2$  (see inset of Fig. 5 for better visualization) the elbow is declared at  $m^* = 3$  for which  $J_m \approx 1.2$ , at the second of the two subsequent sharp bends, after which the curve stops decreasing substantially. This result is reasonable because PC1 and PC2 explain about 95% of the variance, so we would expect that  $m^* = 3$ . This finding also justifies our choice of  $s = 1$ . However, as  $\beta$  increases, the algorithm becomes ineffective due to the smoothness of the reconstruction error curves. This is well illustrated for the curve relative to  $\beta = 2.6$  where no sharp bends are present. Consequently, the declared elbow at  $m^* = 37$

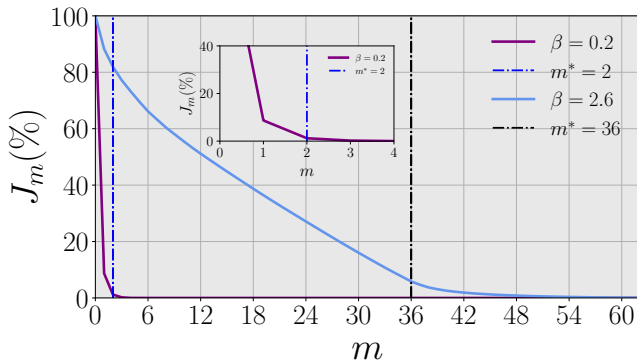


FIG. 5. Kneedle with  $s = 1$  applied to the reconstruction error curve  $J_m$  (in percentage) corresponding to  $\beta = 0.2$  (purple line) and  $\beta = 2.6$  (blue line), obtained from trajectories ( $n_s = 4,000,000$ ) with system size  $N = 32$ , and the initial condition equivalent to giving  $\mathcal{E}_1 \approx 0.45$  to the first mode ( $k = 1, A = 10$ ). Each elbow point is declared at the intersection with the respective vertical line. We set the horizontal axis to zero at  $m = 1$  for better visualization. (Inset) A zoomed-in view of the declared knee point of the curve relative to  $\beta = 0.2$ .

( $J_m \approx 5.8$ ), corresponds to the maximum curvature, but not certainly to an elbow point. We also note in contrast to the other approach, Kneedle yields the same intrinsic dimensions for the curves corresponding to  $\beta = 1$  and  $\beta = 1.1$ , despite it appearing impossible according to the quite different trends of respective reconstruction error curves (see Fig. 3) [62].

On the other hand, the threshold-based approach yields  $m^* \rightarrow 63$  for  $\beta \rightarrow 3$ . This result means that the manifold  $\Sigma_E$  can be approximated by suitable hyperplanes of rank  $n - 1$  at strong nonlinearities. However, this is likely due to the threshold chosen to match the asymptotic values of the analyzed curves. Nevertheless, this approach produces dimensions consistent with those observed through visual inspection.

In the following, we explain how the observed asymptotic trends of  $m^*$  correspond to the specific dynamical features of the  $\beta$  model with  $N = 32$ , namely recurrences ( $\beta \lesssim 1$ ) and mixing ( $\beta \rightarrow 3$ ). To this end, here we recall the analysis of the  $\beta$  model's dynamics with  $N = 32$  and the same initial condition ( $k = 1, A = 10$ ), using the phase plots (or equivalently, the Poincaré maps [63]). Accordingly, the phase plots were applied to the trajectories crossing the hyperplane of equation  $a_3 = 0$ , thereby forming characteristic scatterplots with coordinates  $(a_1, \dot{a}_1)$  [45]. It was found that the scatterplots exhibit well-defined, hexagon-like patterns, consistent with periodic or quasi-periodic motion, resulting in the observed recurrence phenomenon for small values of  $\beta$ . Similar but more complex patterns persist until  $\beta$  approaches unity. Therefore, the system continues to undergo recurrent motion, preventing the energy modes from sharing their energies. However, some significant changes are observed when  $1 < \beta \leq 3$  where evident randomness appears in the scatterplots.

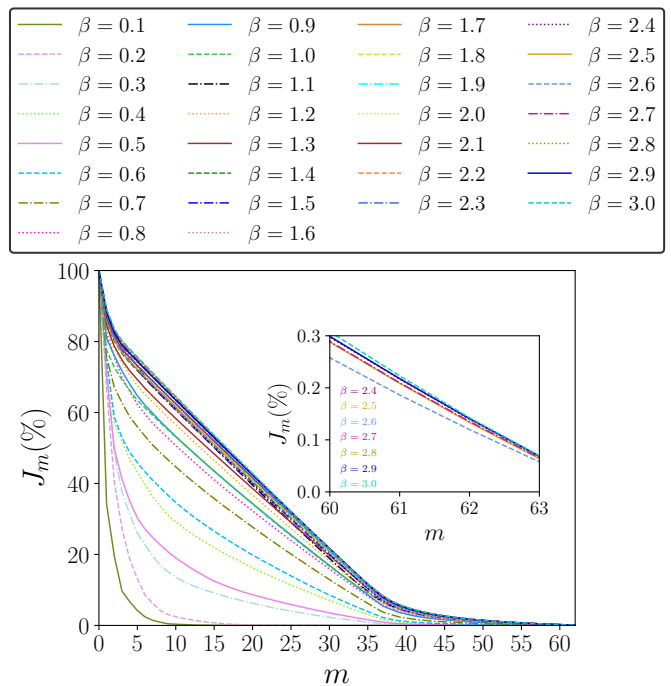


FIG. 6. Reconstruction error  $J_m$  in percentage (%) as a function of the dimension  $m$  of the best-fitting subspace  $U$  for  $\beta \in [0.1, 3]$ , using trajectories of  $N = 32$  coupled oscillators, consisting of  $n_s = 4,000,000$  datapoints, assuming the initial condition equivalent to giving the energy  $\mathcal{E}_1 \approx 0.45$  to the second mode ( $k = 2, A = 10$ ). Note that the zero of the horizontal axis is set at  $m = 1$ . (Inset) The same plot for  $m \in [60, 63]$  shows the curves corresponding to  $\beta \in [2.4, 3]$ .

The latter findings strongly suggest that the system is approaching a chaotic regime as  $\beta$  increases [45]. In such a case, it is observed that the first normal mode efficiently shares its energy irreversibly.

We attempted to confirm the phase plot analysis in a quick and dirty way by studying the time-dependence of the Euclidean distance  $d$  of the system's phase point from the origin of the phase space, during the time evolution (see Sec V C for details). Fig. 15 shows  $d$  as a function of  $t$ , whose values are sampled at intervals of size 20,000. The panels with  $\beta = 0.1, 0.5, 1$  exhibit a clear quasi-periodic pattern. However, as  $\beta$  increases ( $\beta \gtrsim 1.1$ ), the periodic patterns gradually diminish over time, for instance, see the panels with  $\beta = 1.1, 1.2$ , and eventually disappear entirely for larger values of  $\beta$ . This Euclidean metric-based approach, therefore, appears to support the phase plot analysis.

Next, to see the effect of strong nonlinearities on the data dimensionality, we shall apply PCA to trajectory data sets ( $n_s = 4,000,000$ ) where the initial condition is equivalent to giving the energy  $\mathcal{E}_2 \approx 1.8$  to the second normal mode ( $k = 2, A = 10$ ) (see Fig. 9). In such a case, for the same  $\beta$  value, the nonlinearity is stronger by at least a factor of four, due to a greater energy density as explained in Sec. 4. Our quick and dirty Euclidean

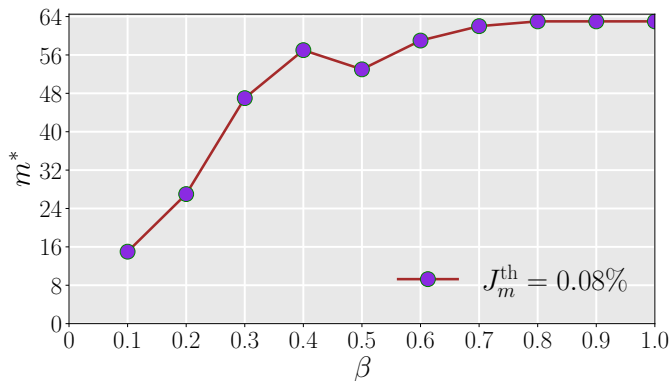


FIG. 7. The estimated intrinsic dimension  $m^*$  of entire trajectories ( $n_s = 4,000,000$ ) with system size  $N = 32$ , and the initial condition equivalent to giving the energy  $\mathcal{E}_2 \approx 1.8$  to the first mode ( $k = 2, A = 10$ ), as a function of  $\beta$ . The dimensions are computed assuming the threshold  $J_m^{\text{th}} = 0.08\%$ .

metric-based analysis applied to trajectory data under scrutiny is shown in Fig. 16. It is found that recurrent motion can be expected only for  $\beta \approx 0$  because no evident periodic patterns emerge across the entire range of  $\beta$ , except for  $\beta = 0.1$ . To further confirm the metric-based analysis, we plot  $E_k$  as a function of  $t$  in Figs. 10, 11, 12, 13, computed from the numerical simulations, assuming  $\beta = 0.1, 0.2, 0.3, 0.4$ , respectively. Energy recurrence is observed throughout the entire time evolution only for  $\beta = 0.1$ . In all other cases, there is always mixing following a phase of recurrent motion, which tends to diminish as  $\beta$  increases. The primary reason is that energy sharing between modes becomes more efficient increasing  $\beta$ . As a result, we would expect these trajectories to exhibit higher dimensionality, which is indeed the case.

In Fig. 6,  $J_m$  (in percentage) is shown as a function of  $m$  for each value of  $\beta$  under scrutiny. This time, the curves form a single family characterized by smoothness. Their slow decay suggests consistency with a large intrinsic dimensionality. The typical values of  $J_m$  are approximately 0.06%–0.07% when  $m = 63$  and  $\beta = 3$ . Therefore, following our previous rationale, we set  $J_m^{\text{th}} = 0.08\%$ . Fig. 7 shows  $m^*$  as a function of  $\beta$ , where we limit ourselves to plot their relationship for  $\beta \in [0.1, 1]$  because  $m^* \rightarrow n - 1$  within such an interval. The relationship between  $m^*$  and  $\beta$  is increasingly monotonic, involving much higher intrinsic dimensionalities, in good agreement with our previous observations. In Table II we report the numerical values of  $m^*$  together with the two principal components PC1 and PC2. Note that preserved variance PC1 + PC2  $\lesssim 50\%$ , apart from when  $\beta = 0.1$  where PC1 + PC2 = 79%. These numerical results align with the high dimensionality observed in this case. Then, we can conclude that, according to PCA, trajectories with high intrinsic dimensions arise from strong nonlinearities.

Here, we aim to address a fundamental limitation of PCA for the problem at hand by visualizing the FPUT trajectories in two dimensions using  $t$ -SNE. Such a man-

ifold learning algorithm is widely used for visualizing data in biological research, such as single-cell RNA sequencing data [39], however, it can also be valuable for visualizing other types of data, including data from digital libraries [64].

A given trajectory data set  $\mathcal{X} = \{x_1, x_2, \dots, x_{n_s}\}$ , will be mapped to the two-dimensional data set  $\mathcal{Y} = \{y_1, y_2, \dots, y_{n_s}\}$ , called map or embedding, by  $t$ -SNE, preserving both local and global structures of the high-dimensional data. However, maintaining the global structure is crucial to provide an informative initialization to the algorithm. Recently, Kobak and Linderman showed that PCA initialization should be used to this end [40]. Additionally, PCA initialization in contrast to random initialization, guarantees the reproducibility of our findings.

The computations will be performed through the implementation of openTSNE [65], keeping all optimization parameters at their default values, e.g., the algorithm was run with the regular early exaggeration phase 12 for 250 iterations, then in the regular (or normal) regime with no exaggeration for 500 iterations. Computations were performed using either  $\mathcal{P} = 30$  or  $\mathcal{P} = 50$ . However, we found that both values yield the same results qualitatively (see discussion below).

Although our  $t$ -SNE implementation can visualize several million data points, we will limit our analysis to small, complete trajectories generated during the early-stage dynamics. The main reasons for this choice are as follows. First, embeddings from large trajectory data sets exhibit overly complex patterns, making them difficult to interpret. Second, we are specifically interested in orbits exhibiting periodic or quasi-periodic motion, which arise when  $\beta \lesssim 1.0$  and the initial condition involves exciting the first mode ( $k = 1, A = 10$ ). To this end, trajectories with  $n_s = 10^3, 10^4$ , generated during the early-stage dynamics, are sufficient.

In Fig. 8  $t$ -SNE embeddings ( $\mathcal{P} = 50$ ) of the entire orbits, with  $n_s = 10,000$  and  $n_s = 2,000$  datapoints corresponding to  $\beta = 0.1$  and  $\beta = 0.5, 1$ , respectively, are shown. Throughout PCA initialization was used. The top panels (a), (b), (c) and bottom panels (d), (e), (f) show the embeddings obtained using Euclidean distance and cosine similarity, respectively. The embeddings correctly reproduce the quasi-periodicity of motion as expected for the high-dimensional trajectories, thereby confirming the phase plot analysis and observed energy recurrences in the dynamical regime for which  $\beta \lesssim 1$ . Note that Euclidean and cosine similarity yield qualitatively similar embeddings.

Note that without the PCA initialization, it would be impossible to obtain such meaningful embeddings. This fact is illustrated in Fig. 17 where  $t$ -SNE embeddings were computed with random initialization. In this case, the algorithm produces a knot for  $\beta = 0.1$  (panels (a) and (d)) and some disconnected curves for  $\beta = 0.5, 1$  (panels (b) and (c)), respectively. There is no periodic pattern in such embeddings. Additionally, from a general point

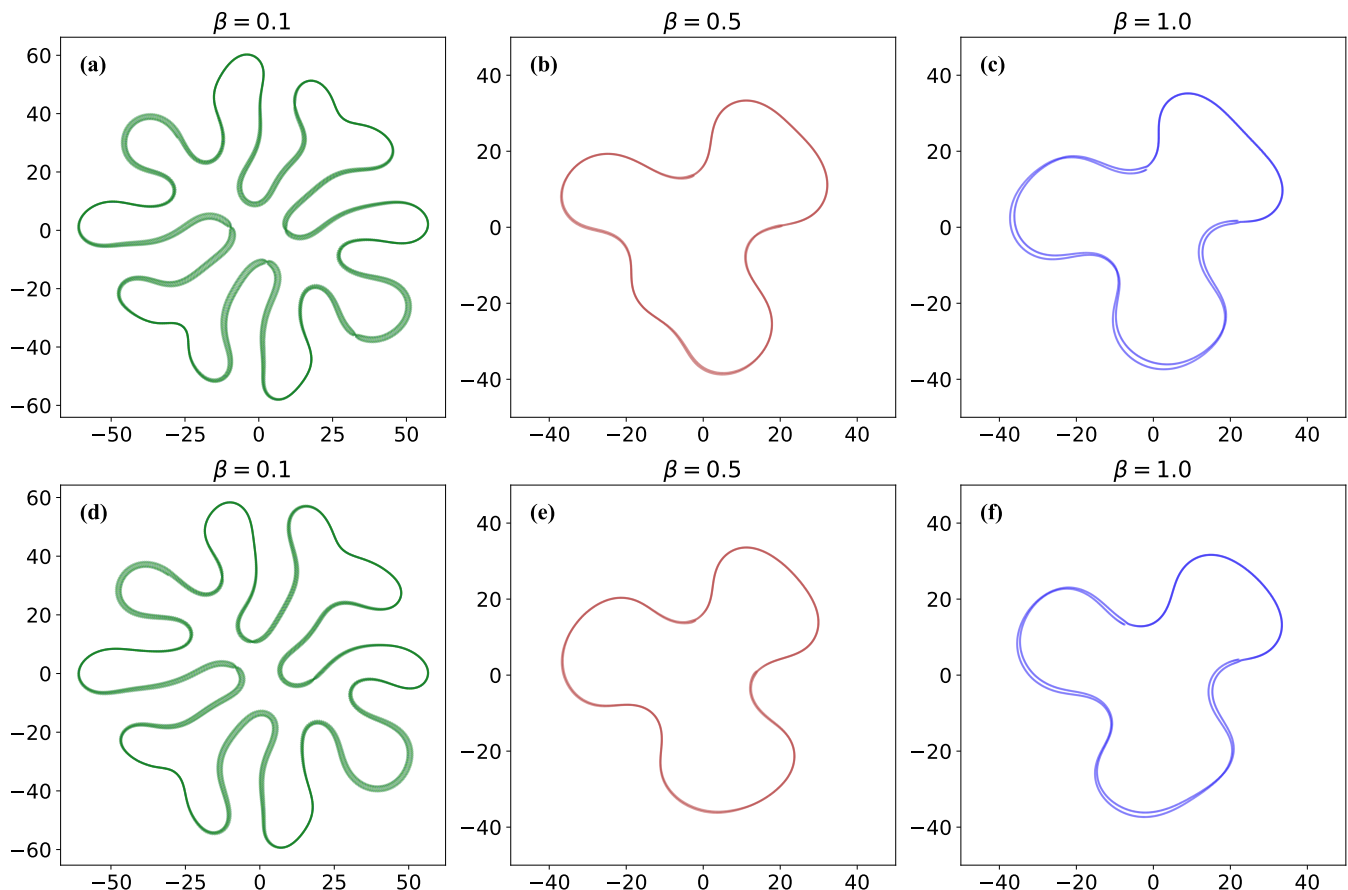


FIG. 8.  $t$ -SNE embeddings of the entire trajectories of early-stage dynamics, with  $n_s = 10,000$  and  $n_s = 2,000$  datapoints corresponding to  $\beta = 0.1$  and  $\beta = 0.5, 1$ , respectively. The top panels (a), (b), (c) and bottom panels (d), (e), (f) show embeddings obtained using Euclidean distance and cosine similarity, respectively. PCA initialization was used throughout, with a perplexity  $\mathcal{P} = 50$ .

of view, these embeddings cannot faithfully represent an entire high-dimensional orbit, as the latter consists of only one connected component.

Regarding our choice of perplexity, we found that setting  $\mathcal{P} = 30$  (see Fig. 18) produces qualitatively similar embeddings, confirming that the algorithm’s performance is robust to variations in  $\mathcal{P}$ .

We conclude with an important observation about our findings. Similar embeddings to those for  $\beta = 0.1$  can be obtained by applying  $t$ -SNE to points sampled from a circle with a small amount of Gaussian noise [40]. This observation strongly suggests that the datapoints lie near or on a curved one-dimensional manifold, during the early-stage dynamics for weak nonlinearities. Consequently, PCA may fail in the weak nonlinearity regime, similar to what occurs when applied to datapoints representing a person’s movement on a Ferris wheel [32, 34] or those forming the “Swiss roll” synthetic data set [30, 56].

## V. CONCLUSION AND OUTLOOK

In summary, the principal component analysis can reveal a meaningful relationship between the intrinsic dimensionality of trajectories and the model’s nonlinear strength. According to PCA,  $m^* \ll n$  for weak nonlinearities and  $m^* \rightarrow n - 1$  for strong nonlinearities.

However, PCA approach yields inaccurate dimensionality estimates. First, the finding  $m^* = n - 1$  likely depends on our specific choice of threshold for the reconstruction error. Second, the values of  $m^*$  are likely underestimated for small nonlinearities. PCA assumes that datapoints are distributed near a low-dimensional linear manifold, or hyperplane, which does not seem to hold in our analysis using  $t$ -SNE on the trajectory data for recurrent motion ( $\beta \lesssim 1$ ), beginning from the initially excited first mode ( $k = 1, A = 10$ ).

That being said, different machine learning algorithms could improve the current estimates. For instance, this task may be achieved through kernel PCA [66], which utilizes the kernel trick—an implicit transformation of the input data—to address data nonlinearity. However,



this approach requires selecting an appropriate kernel (e.g., the Gaussian kernel) and tuning hyperparameters, such as the kernel's length scale and regularization strength [56, 67]. Additionally, other manifold reduction algorithms are available; see Ref. [68] and references therein. Nevertheless, we believe that neural network architectures like autoencoders, which capture complex nonlinear correlations using activation functions such as the sigmoid, could be ideal for overcoming the capabilities of PCA [33, 41, 42, 68].

For future work, attention should be directed towards studying the  $\beta$  model with larger system size, e.g.,  $N = 64$ ,  $N = 128$ , or exploring other FPUT variants, such as the  $\alpha$  model and the combined  $\alpha + \beta$  model. However, the trajectory data size  $n_s$  should be chosen carefully to ensure it contains all relevant dynamical information for the model under study. Furthermore, with some caution, manifold learning from data across multiple trajectories may also prove useful.

Finally, there is strong evidence supporting the existence of a nonlinear manifold for the trajectory data generated in recurrent motion. This manifold could be effectively investigated through topological data analysis (TDA) [69–72] or geometric data analysis (GDA) [73]. For instance, persistent homology, a tool from TDA, could, in principle, measure the number of connected components,

holes, and higher-dimensional voids in the data. Similarly, GDA can extract useful information by examining geometric invariants of a manifold, such as its curvature [74].

## Acknowledgements

I thank Dmitry Kobak for helpful correspondence during the preparation of this article and for suggesting the use of the Python library openTSNE [65], and Giancarlo Benettin for correspondence about the FPUT model. The author is also indebted with Jack Dongarra and David Keyes for providing their recent review paper [5].

## Data Availability

The data studied in this article including energies and distances will be available on Zenodo (<https://zenodo.org/>) under an open-source Creative Commons Attribution license.

## Code Availability

Code for simulations and machine learning computations will be available upon reasonable request to the author on GitHub at [75].

- 
- [1] E. Fermi, J. Pasta, S. Ulam, and M. Tsingou, Studies of nonlinear problems i, Los Alamos preprint LA-1940 (1955).
- [2] J. Ford, The fermi-pasta-ulam problem: Paradox turns discovery, *Physics Reports* **213**, 271 (1992).
- [3] T. P. Weissert, *The Genesis of Simulation in Dynamics. Pursuing the Fermi-Pasta-Ulam Problem*, 1st ed. (Springer, New York, NY, 1997).
- [4] M. Falcioni and A. Vulpiani, Enrico fermis's contribution to non-linear systems: The influence of an unpublished article, in *Enrico Fermi: His Work and Legacy*, edited by C. Bernardini and L. Bonolis (Springer Berlin Heidelberg, Berlin, Heidelberg, 2004) pp. 271–285.
- [5] J. Dongarra and D. Keyes, The co-evolution of computational physics and high-performance computing, *Nature Reviews Physics* (2024).
- [6] H. L. Anderson, Scientific uses of the maniac, *Journal of Statistical Physics* **43**, 731 (1986).
- [7] M. A. Porter, N. J. Zabusky, B. Hu, and D. K. Campbell, Fermi, pasta, ulam and the birth of experimental mathematics, *American Scientist* **97**, 214 (2009).
- [8] G. Gallavotti, *Nonequilibrium and Irreversibility*, 1st ed. (Springer Cham, Heidelberg, 2014).
- [9] Z. Liu and M. Tegmark, Machine learning conservation laws from trajectories, *Phys. Rev. Lett.* **126**, 180604 (2021).
- [10] C. C. Moore, Ergodic theorem, ergodic theory, and statistical mechanics, *Proceedings of the National Academy of Sciences* **112**, 1907 (2015).
- [11] What Boltzmann meant with ergodic hypothesis probably was what is referred to as Ehrenfest's quasi-ergodic hypothesis.
- [12] T. D. Kühne, M. Iannuzzi, M. Del Ben, V. V. Rybkin, P. Seewald, F. Stein, T. Laino, R. Z. Khaliullin, O. Schütt, F. Schiffmann, D. Golze, J. Wilhelm, S. Chulkov, M. H. Bani-Hashemian, V. Weber, U. Borštnik, M. Taillefumier, A. S. Jakobovits, A. Lazzaro, H. Pabst, T. Müller, R. Schade, M. Guidon, S. Andermatt, N. Holmberg, G. K. Schenter, A. Hehn, A. Bussy, F. Belleflamme, G. Tabacchi, A. Glöß, M. Lass, I. Bethune, C. J. Mundy, C. Plessl, M. Watkins, J. VandeVondele, M. Krack, and J. Hutter, CP2K: An electronic structure and molecular dynamics software package - Quickstep: Efficient and accurate electronic structure calculations, *The Journal of Chemical Physics* **152**, 194103 (2020).
- [13] D. Frenkel and B. Smit, *Understanding molecular simulation: from algorithms to applications* (Academic Press, 2002).
- [14] J. Tuck and M. Menzel, The superperiod of the nonlinear weighted string (fpu) problem, *Advances in Mathematics* **9**, 399 (1972).
- [15] F. M. Izrailev and B. V. Chirikov, Statistical properties of a nonlinear string, *Soviet Physics Doklady* **11**, 30 (1966).
- [16] Fucito, F., Marchesoni, F., Marinari, E., Parisi, G., Peliti, L., Ruffo, S., and Vulpiani, A., Approach to equilibrium in a chain of nonlinear oscillators, *J. Phys. France* **43**, 707 (1982).
- [17] G. P. Berman and F. M. Izrailev, The Fermi–Pasta–Ulam problem: Fifty years of progress, *Chaos: An Interdisciplinary Journal of Nonlinear Science* **15**, 015104 (2005).
- [18] T. Penati and S. Flach, Tail resonances of Fermi-Pasta-Ulam q-breathers and their impact on the pathway to

- equipartition, *Chaos: An Interdisciplinary Journal of Nonlinear Science* **17**, 023102 (2007).
- [19] M. Onorato, L. Vozella, D. Proment, and Y. V. Lvov, A route to thermalization in the  $\alpha$ -fermi-pasta-ulam system, *Proceedings of the National Academy of Sciences* **112**, 4208 (2015).
- [20] V. I. Arnold, *Mathematical Methods of Classical Mechanics*, 2nd ed. (Springer-Verlag, New York, NY, 1989).
- [21] B. Rink, Symmetric invariant manifolds in the fermi-pasta-ulam lattice, *Physica D: Nonlinear Phenomena* **175**, 31 (2003).
- [22] J. Masoliver and A. Ros, Integrability and chaos: the classical uncertainty, *European Journal of Physics* **32**, 431 (2011).
- [23] N. Karve, N. Rose, and D. Campbell, Periodic orbits in Fermi-Pasta-Ulam-Tsingou systems, *Chaos: An Interdisciplinary Journal of Nonlinear Science* **34**, 093117 (2024).
- [24] K. Huang, *Statistical Mechanics*, 2nd ed. (John Wiley & Sons, New York, 1987).
- [25] T. Hastie, R. Tibshirani, and J. Friedman, *The Elements of Statistical Learning*, 12th ed., Springer Series in Statistics (Springer New York Inc., New York, NY, USA, 2017).
- [26] I. T. Jolliffe and J. Cadima, Principal component analysis: a review and recent developments, *Philosophical Transactions of the Royal Society A: Mathematical, Physical and Engineering Sciences* **374**, 20150202 (2016).
- [27] M. P. Deisenroth, A. A. Faisal, and C. S. Ong, *Mathematics for Machine Learning* (Cambridge University Press, 2020).
- [28] L. Verlet, Computer "experiments" on classical fluids: Thermodynamical properties of lennard-jones molecules, *Phys. Rev.* **159**, 98 (1967).
- [29] E. Hairer, G. Wanner, and C. Lubich, Symplectic integration of hamiltonian systems, in *Geometric Numerical Integration: Structure-Preserving Algorithms for Ordinary Differential Equations* (Springer Berlin Heidelberg, Berlin, Heidelberg, 2006) pp. 179–236.
- [30] J. B. Tenenbaum, V. de Silva, and J. C. Langford, A global geometric framework for nonlinear dimensionality reduction, *Science* **290**, 2319 (2000).
- [31] V. Satopaa, J. Albrecht, D. Irwin, and B. Raghavan, Finding a "kneedle" in a haystack: Detecting knee points in system behavior, in *2011 31st International Conference on Distributed Computing Systems Workshops* (2011) pp. 166–171.
- [32] L. Agostini, Exploration and prediction of fluid dynamical systems using auto-encoder technology, *Physics of Fluids* **32**, 067103 (2020).
- [33] A. Glielmo, B. E. Husic, A. Rodriguez, C. Clementi, F. Noé, and A. Laio, Unsupervised learning methods for molecular simulation data, *Chemical Reviews* **121**, 9722 (2021).
- [34] J. Shlens, A tutorial on principal component analysis (2014), [arXiv:1404.1100 \[cs.LG\]](https://arxiv.org/abs/1404.1100).
- [35] PCA is not robust to the outliers.
- [36] In literature,  $t$ -SNE is commonly referred to as a nonlinear manifold reduction algorithm.
- [37] L. van der Maaten and G. Hinton, Visualizing data using t-sne, *Journal of Machine Learning Research* **9**, 2579 (2008).
- [38] G. C. Linderman and S. Steinerberger, Clustering with t-sne, provably, *SIAM Journal on Mathematics of Data Science* **1**, 313 (2019).
- [39] D. Kobak and P. Berens, The art of using t-sne for single-cell transcriptomics, *Nature Communications* **10**, 5416 (2019).
- [40] D. Kobak and G. C. Linderman, Initialization is critical for preserving global data structure in both t-sne and umap, *Nature Biotechnology* **39**, 156 (2021).
- [41] C. Wehmeyer and F. Noé, Time-lagged autoencoders: Deep learning of slow collective variables for molecular kinetics, *The Journal of Chemical Physics* **148**, 241703 (2018).
- [42] S. E. Otto and C. W. Rowley, Linearly recurrent autoencoder networks for learning dynamics, *SIAM Journal on Applied Dynamical Systems* **18**, 558 (2019).
- [43] G. Benettin, H. Christodoulidi, and A. Ponno, *Journal of Statistical Physics* **152**, 195 (2013).
- [44] G. Benettin, (Private Communication).
- [45] N. J. Giordano and H. Nakanishi, *Computational Physics*, 2nd ed. (Pearson Prentice Hall, 2006).
- [46] S. D. Pace, K. A. Reiss, and D. K. Campbell, The Fermi-Pasta-Ulam-Tsingou recurrence problem, *Chaos: An Interdisciplinary Journal of Nonlinear Science* **29**, 113107 (2019).
- [47] K. A. Reiss and D. K. Campbell, The metastable state of fermi-pasta-ulam-tsingou models, *Entropy* **25** (2023).
- [48] From the Hamiltonian  $H$  follows the canonical equations:  $\dot{q} = \partial H / \partial p$ ,  $\dot{p} = -\partial H / \partial q$ .
- [49] G. Benettin and A. Ponno, On the numerical integration of fpu-like systems, *Physica D: Nonlinear Phenomena* **240**, 568 (2011).
- [50] P. K. Eastman and V. S. Pande, Energy conservation as a measure of simulation accuracy, *bioRxiv* (2016).
- [51] K. Pearson, On lines and planes of closest fit to systems of points in space, *Philosophical Magazine Series 1* **2**, 559 (1901).
- [52] H. Hotelling, Analysis of a complex of statistical variables into principal components., *Journal of Educational Psychology* **24**, 498 (1933).
- [53] G. Strang, The fundamental theorem of linear algebra, *The American Mathematical Monthly* **100**, 848 (1993).
- [54] G. W. Stewart, On the early history of the singular value decomposition, *SIAM Review* **35**, 551 (1993).
- [55] F. Pedregosa, G. Varoquaux, A. Gramfort, V. Michel, B. Thirion, O. Grisel, M. Blondel, P. Prettenhofer, R. Weiss, V. Dubourg, J. Vanderplas, A. Passos, D. Cournapeau, M. Brucher, M. Perrot, and Édouard Duchesnay, Scikit-learn: Machine learning in python, *Journal of Machine Learning Research* **12**, 2825 (2011).
- [56] A. Géron, *Hands-On Machine Learning with Scikit-Learn and TensorFlow: Concepts, Tools, and Techniques to Build Intelligent Systems* (O'Reilly, U.S.A, 2019).
- [57] In other words, the perplexity defines the scale on which points can be considered close.
- [58] D. Kobak, (Private Communication).
- [59] The variables  $q, p$ , commonly referred to as features, are centered around zero with a standard deviation set to unity. The latter ensures that all variables have equal importance in the analysis.
- [60] D. J. Ketchen and C. L. Shook, The application of cluster analysis in strategic management research: An analysis and critique, *Strategic Management Journal* **17**, 441 (1996).
- [61] Elbows (knees) can appear in curves with negative (positive) concavity. For instance, knees are typically observed in the explained variance curves of PCA.

- [62] Although irrelevant, we note a large discrepancy that arises for  $\beta = 2.3$ , yielding  $m^* = 20$ . We presume this is due to a numerical error in the Python package implementing Kneedle (<https://pypi.org/project/kneed/>), which we used for our computations.
- [63] W. Tucker, Computing accurate poincaré maps, *Physica D: Nonlinear Phenomena* **171**, 127 (2002).
- [64] B. M. Schmidt, Stable random projection: Lightweight, general-purpose dimensionality reduction for digitized libraries, *Journal of Cultural Analytics* (2018).
- [65] P. G. Poličar, M. Stražar, and B. Zupan, opentsne: A modular python library for t-sne dimensionality reduction and embedding, *Journal of Statistical Software* **109**, 1–30 (2024).
- [66] B. Schölkopf, A. Smola, and K.-R. Müller, Nonlinear Component Analysis as a Kernel Eigenvalue Problem, *Neural Computation* **10**, 1299 (1998).
- [67] M. Rupp, Machine learning for quantum mechanics in a nutshell, *International Journal of Quantum Chemistry* **115**, 1058 (2015).
- [68] L. Bonheme and M. Grzes, [Fondue: an algorithm to find the optimal dimensionality of the latent representations of variational autoencoders](#) (2022), [arXiv:2209.12806 \[cs.LG\]](#).
- [69] G. E. Carlsson, Topology and data, *Bulletin of the American Mathematical Society* **46**, 255 (2009).
- [70] E. Munch, A user’s guide to topological data analysis, *Journal of Learning Analytics* **4**, 47–61 (2017).
- [71] N. Otter, M. A. Porter, U. Tillmann, P. Grindrod, and H. A. Harrington, A roadmap for the computation of persistent homology, *EPJ Data Science* **6**, 17 (2017).
- [72] F. Chazal and B. Michel, An introduction to topological data analysis: Fundamental and practical aspects for data scientists, *Frontiers in Artificial Intelligence* **4** (2021).
- [73] A. Hickok, *Topics in Geometric and Topological Data Analysis*, Phd thesis, University of California, Los Angeles (2023), available at <https://escholarship.org/uc/item/4h6345xq>.
- [74] A. Hickok and A. J. Blumberg, [An intrinsic approach to scalar-curvature estimation for point clouds](#) (2023), [arXiv:2308.02615 \[stat.ML\]](#).
- [75] <https://github.com/GionniMarchettiMInstP>.

## SUPPLEMENTARY INFORMATION

### A. Initial Conditions and Simulations

The FPUT trajectories under scrutiny start either from the initially excited first mode or from the initially excited second mode, computed, setting  $k = 1, A = 10$  and  $k = 2, A = 10$  into Eq. 4, respectively. These initial conditions correspond to initially displacing the coordinates  $q_i$  ( $i = 1, \dots, 32$ ) as depicted in Fig. 9 with a solid ( $k = 1, A = 10$ ) and dashed line ( $k = 2, A = 10$ ). The initial conditions for variables  $p_i$  are  $p_i = 0$  with  $i = 1, \dots, 32$ .

The linear system's energy takes the values  $\mathcal{E}_1 \approx 0.45$  and  $\mathcal{E}_2 \approx 1.8$  when  $k = 1, A = 10$  and  $k = 2, A = 10$ , respectively.

Here, it is worth noting that assuming weak non-linearity, i.e.,  $\beta \approx 0$ , the system's energy density is  $\epsilon_1 \approx 14 \times 10^{-3}$  and  $\epsilon_2 \approx 56 \times 10^{-3}$ , for  $k = 1$  and  $k = 2$ , respectively. As a result,  $\epsilon_2 \approx 4\epsilon_1$ . Therefore the system's motion starting from the initially excited second mode is affected by a stronger nonlinearity for a given  $\beta$  than that starting from the initially excited first mode.

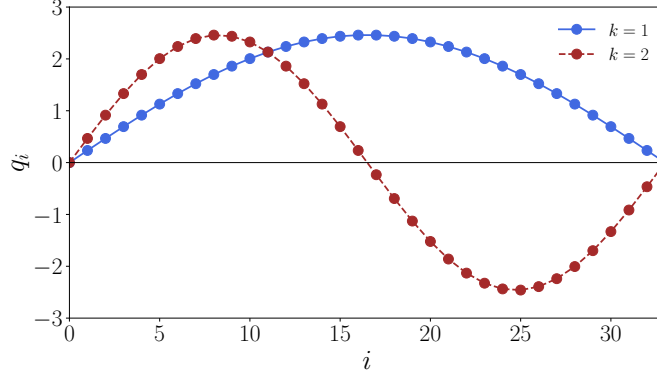


FIG. 9. The coordinates  $q_i$  ( $i = 1, \dots, 32$ ) at time  $t = 0$  according to Eq. 4, assuming to initially exciting the first mode  $k = 1$  (solid line) or the second mode  $k = 2$  (dashed line). In both cases  $A = 10$ .

### B. PCA Results

In Fig. 14, the eigenvalues  $\lambda_i$  that yield the preserved variance along the principal components (PCs) are shown as functions of the number of PCs. In such a case, we applied the SVD to the standardized version of the data matrix  $X$  constructed with the data points belonging to entire trajectories ( $n_s = 4,000,000$ ), starting from the first excited mode ( $k = 1, A = 10$ ).

Note that the trends of  $\lambda_i$  provide the variance perspective of PCA. For instance, when  $\beta = 0.1$ , only  $\lambda_1$  and  $\lambda_2$  differ significantly from zero. As a result, the sum of the first two principal components PC1 and PC2 must preserve about 100% of the data variance. This fact is numerically confirmed as PC1 = 50% and PC2 = 49% (see Table I).

Tables I and II display the first two principal components, PC1 and PC2, their respective sums, the maximum reconstruction error  $J_m^{\max}$ , and the estimated effective dimension  $m^*$  for trajectory data corresponding to the initial conditions: first excited mode ( $k = 1, A = 10$ ) and second excited mode ( $k = 2, A = 10$ ), respectively.

### C. Euclidean Distance

In the case of  $k = 1$ , the recurrences observed for  $\beta \lesssim 1$  stem from the system's quasi-periodic motion. Consequently, there is a possibility of observing time-dependent periodic patterns in observables other than the mode energies. Accordingly, we chose to compute the time-dependence of Euclidean distance  $d$  between the phase points belonging to a given trajectory from the origin of phase space  $\mathbb{R}^{64}$ , taking the latter as a reference point. In such a case it may be convenient to think of the trajectory data set  $\mathcal{X} = \{x_1, x_2, \dots, x_{n_s}\}$  as  $\mathcal{S} = \{x(t) | t \geq 0\}$  for which  $x(0) = x_1$ . In Fig. 15 (Fig. 16)  $d$  is shown as a function of time  $t$  for each value of  $\beta$  under scrutiny, assuming the initial condition corresponding to  $k = 1, A = 10$  ( $k = 2, A = 10$ ). Note that, for better visualization, only the values of  $d$  sampled at time intervals of size 20,000 are plotted.

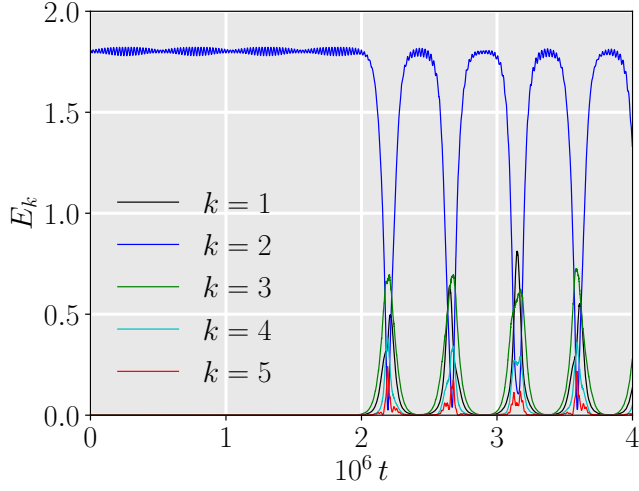


FIG. 10. The energy  $E_k$  of modes with  $k = 1, 2, 3, 4, 5$  as a function of the time  $t$  for  $\beta$  model with  $\beta = 0.1$  assuming  $N = 32$ . The system's equations of motion were numerically integrated with step size  $h = 0.05$ . The initial condition is set to provide the energy  $\mathcal{E} \approx 1.8$  to the second normal mode ( $k = 2, A = 10$ ).

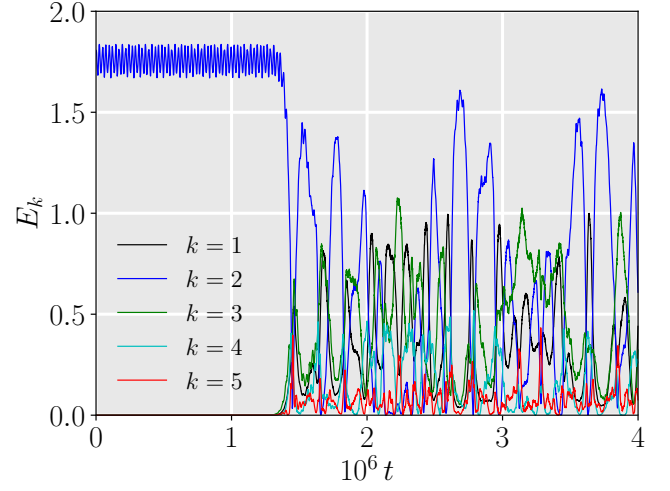


FIG. 11. The energy  $E_k$  of modes with  $k = 1, 2, 3, 4, 5$  as a function of the time  $t$  for  $\beta$  model with  $\beta = 0.2$  assuming  $N = 32$ . The system's equations of motion were numerically integrated with step size  $h = 0.05$ . The initial condition is set to provide the energy  $\mathcal{E} \approx 1.8$  to the second normal mode ( $k = 2, A = 10$ ).

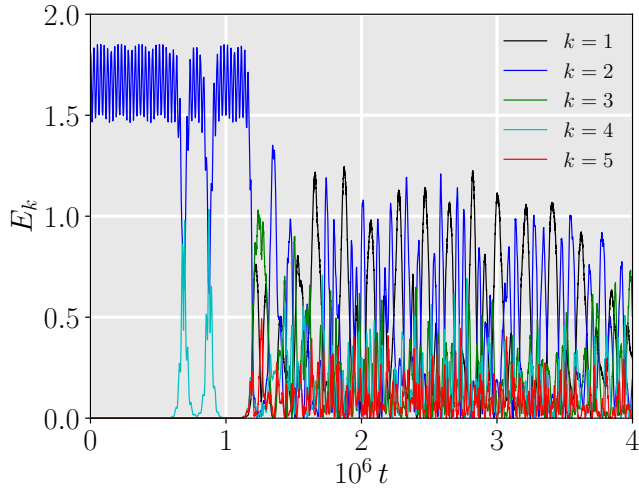


FIG. 12. The energy  $E_k$  of modes with  $k = 1, 2, 3, 4, 5$  as a function of the time  $t$  for  $\beta$  model with  $\beta = 0.3$  assuming  $N = 32$ . The system's equations of motion were numerically integrated with step size  $h = 0.05$ . The initial condition is set to provide the energy  $\mathcal{E} \approx 1.8$  to the second normal mode ( $k = 2, A = 10$ ).

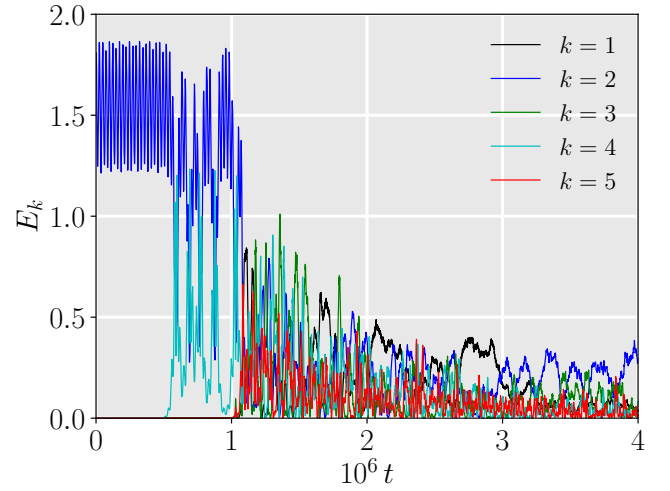


FIG. 13. The energy  $E_k$  of modes with  $k = 1, 2, 3, 4, 5$  as a function of the time  $t$  for  $\beta$  model with  $\beta = 0.4$  assuming  $N = 32$ . The system's equations of motion were numerically integrated with step size  $h = 0.05$ . The initial condition is set to provide the energy  $\mathcal{E} \approx 1.8$  to the second normal mode ( $k = 2, A = 10$ ).

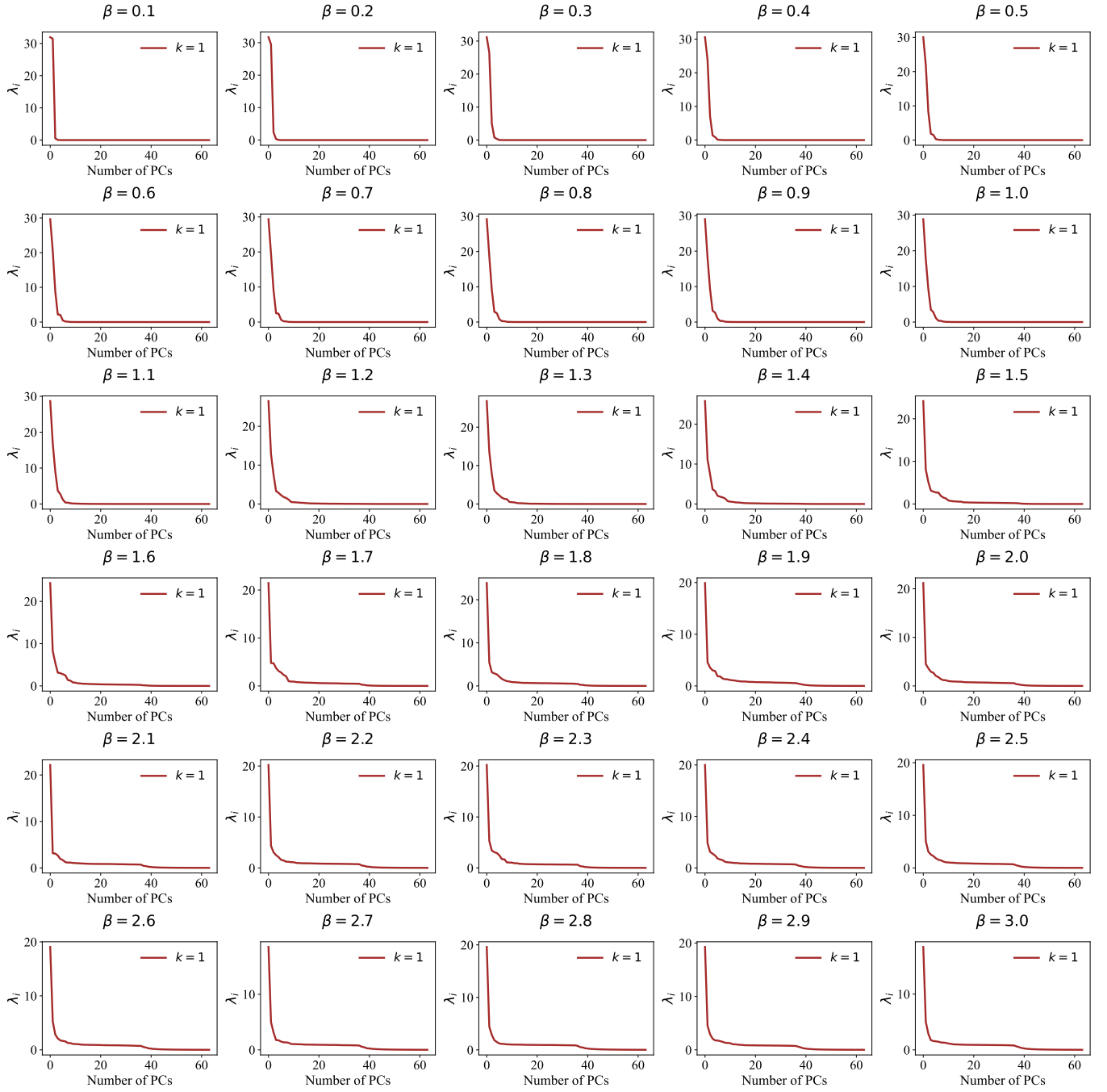


FIG. 14. Eigenvalues  $\lambda_i$  as functions of the number of the principal components PCs according to SVD applied to data from the entire trajectories ( $n_s = 4,000,000$ ), assuming the system size  $N = 32$  and  $\beta \in [0.1, 3]$ . The initial condition of the trajectories corresponds to initially exciting the first mode  $k = 1$  ( $A = 10$ ). Note that the zero of the horizontal axis is set at the first principal component (PC1).

TABLE I. The first two principal components PC1 and PC2 of datasets generated by entire trajectories ( $n_s = 4,000,000$ ) with the initial condition corresponding to initially giving the energy  $\mathcal{E} \approx 0.45$  to the first mode ( $k = 1, A = 10$ ), for each value of  $\beta \in [0.1, 3]$ . In the fourth column the maximum reconstruction error  $J_m^{\max}$  is shown. The last two columns display the estimated intrinsic dimensions  $m_1^*$  and  $m_2^*$ , computed using the threshold-based approach taking  $J_m^{\text{th}} = 0.05\%$  and Kneedle algorithm, respectively.

$\beta$	PC1 (%)	PC2 (%)	PC1 + PC2 (%)	$J_m^{\max}$	$m_1^*$	$m_2^*$
0.1	50	49	99	32.06	4	3
0.2	49	46	95	32.32	5	3
0.3	49	41	90	32.83	7	4
0.4	48	37	85	33.43	8	5
0.5	47	34	81	33.95	9	5
0.6	46	32	78	34.34	10	5
0.7	46	30	76	34.63	11	6
0.8	45	29	74	34.81	11	6
0.9	45	28	73	34.98	13	6
1.0	45	27	72	35.12	13	6
1.1	45	26	71	35.33	27	6
1.2	41	20	61	37.54	44	9
1.3	42	21	63	37.22	40	9
1.4	40	17	57	38.23	46	10
1.5	38	12	50	39.85	54	12
1.6	38	13	51	39.65	55	11
1.7	33	7	40	42.54	60	16
1.8	37	8	45	40.13	60	21
1.9	31	7	38	44.09	62	24
2.0	33	7	40	42.82	61	26
2.1	35	5	40	41.85	62	37
2.2	31	7	38	43.79	63	37
2.3	31	8	39	43.80	62	20
2.4	31	7	38	44.00	62	34
2.5	30	8	38	44.44	63	34
2.6	30	8	38	44.93	63	37
2.7	29	8	37	45.48	63	37
2.8	31	7	38	44.38	63	37
2.9	30	7	37	44.73	63	37
3.0	29	8	37	45.54	63	37

TABLE II. The first two principal components PC1 and PC2 of datasets generated by entire trajectories ( $n_s = 4,000,000$ ) with the initial condition corresponding to giving the energy  $\mathcal{E} \approx 1.8$  to the second mode ( $k = 2, A = 10$ ), for each value of  $\beta \in [0.1, 1]$ . In the fourth column the maximum reconstruction error  $J_m^{\max}$  is shown. The last column displays the estimated intrinsic dimension  $m^*$ , computed using the threshold-based approach taking  $J_m^{\text{th}} = 0.08\%$ .

$\beta$	PC1 (%)	PC2 (%)	PC1 + PC2 (%)	$J_m^{\max}$	$m^*$
0.1	40	39	79	38.29	15
0.2	25	25	50	47.85	27
0.3	25	20	45	47.89	47
0.4	22	21	43	49.94	57
0.5	30	20	50	44.77	53
0.6	24	19	43	48.79	59
0.7	20	19	39	51.34	62
0.8	21	14	35	50.34	63
0.9	23	15	38	49.75	63
1.0	18	18	36	52.17	63



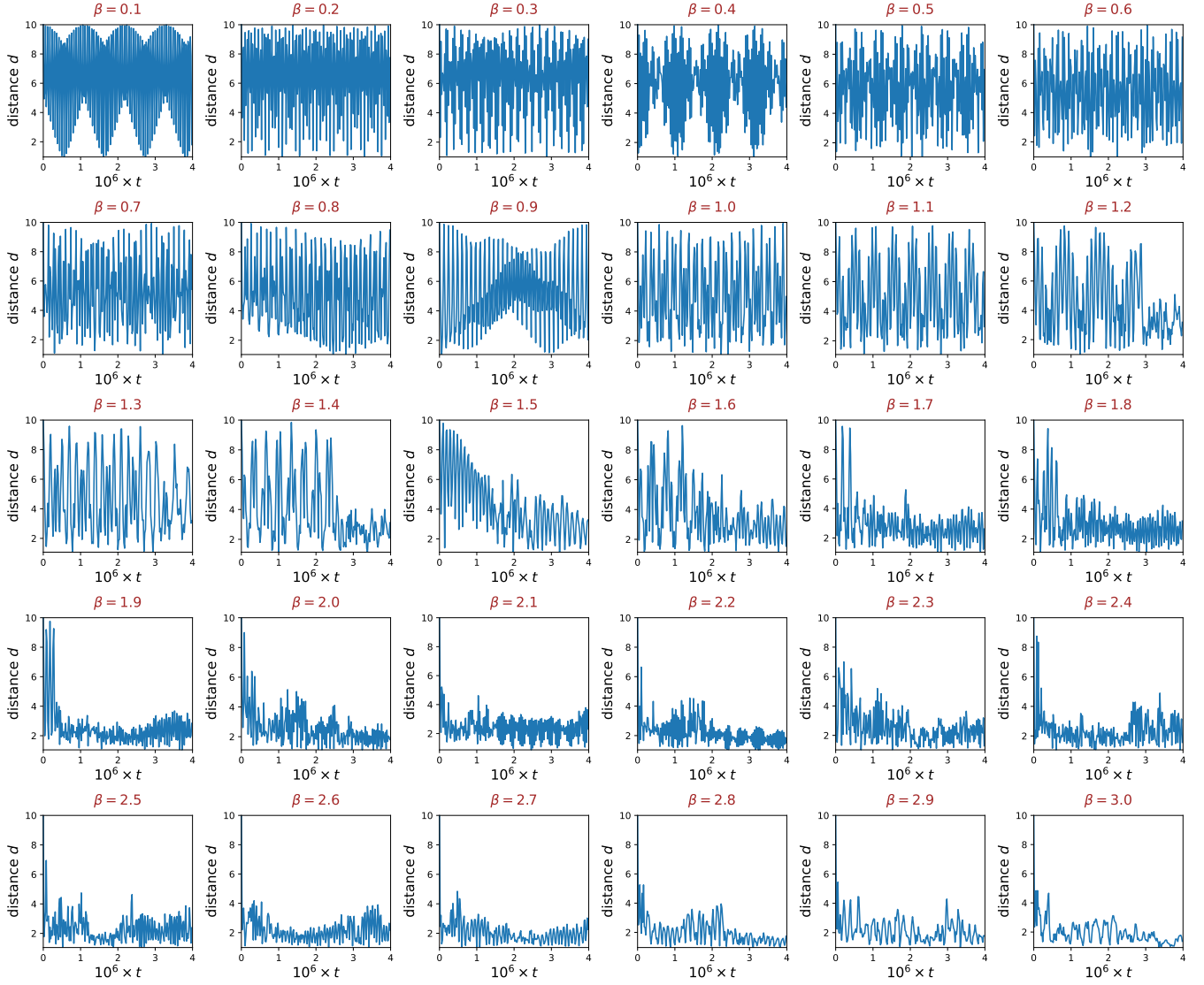


FIG. 15. The Euclidean distance  $d$  between the origin of  $\mathbb{R}^{64}$  and the phase point during the time-evolution of the model with  $N = 32$ , as a function of time for each value of  $\beta$  under scrutiny. All the trajectories ( $n_s = 4,000,000$ ) start with the same initial condition corresponding to giving the energy  $E \approx 0.45$  to the first normal mode ( $k = 1, A = 10$ ). Note that, for visual clarity, only the values of  $d$  taken at multiples of time intervals of size 20,000 are plotted.

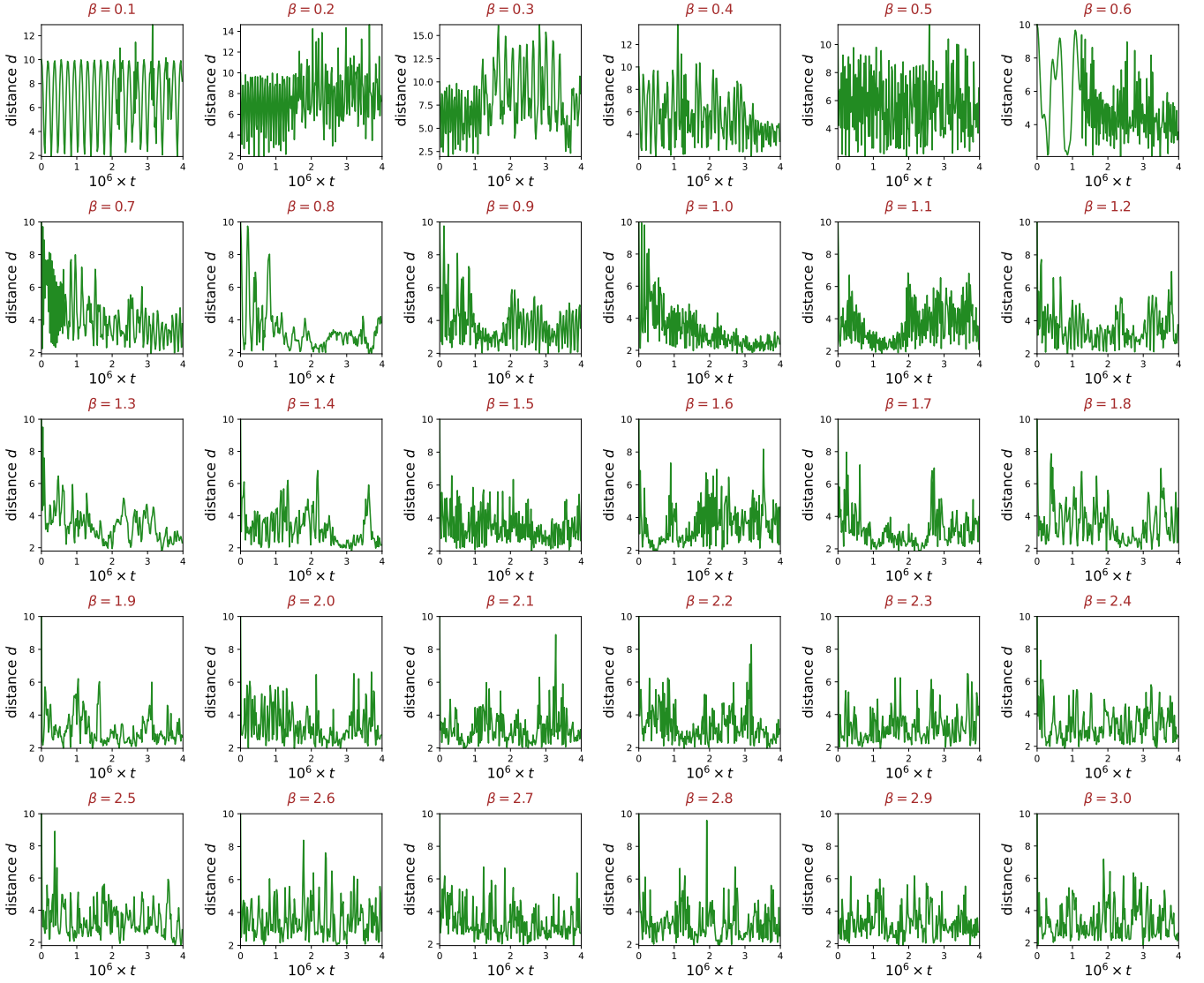


FIG. 16. The Euclidean distance  $d$  between the origin of  $\mathbb{R}^{64}$  and the phase point during the time-evolution of the model with  $N = 32$ , as a function of time for each value of  $\beta$  under scrutiny. All the trajectories ( $n_s = 4,000,000$ ) start with the same initial condition, corresponding to giving the energy  $E \approx 1.8$  to the second normal mode ( $k = 2, A = 10$ ). Note that, for visual clarity, only the values of  $d$  taken at multiples of time intervals of size 20,000 are plotted.

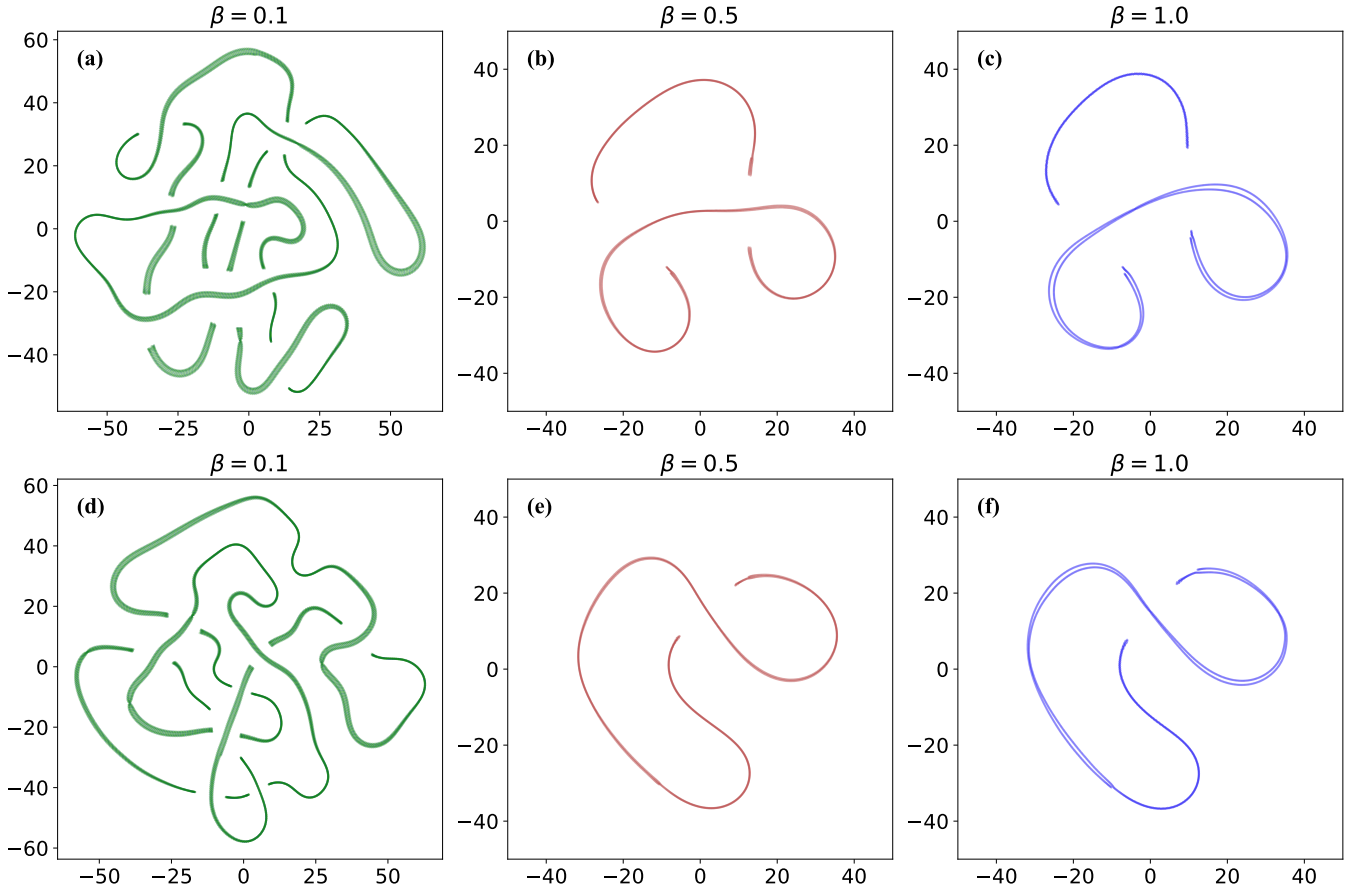


FIG. 17.  $t$ -SNE embeddings of the entire trajectories of early-stage dynamics, with  $n_s = 10,000$  and  $n_s = 2,000$  datapoints corresponding to  $\beta = 0.1$  and  $\beta = 0.5, 1$ , respectively. The top panels (a), (b), (c) and bottom panels (d), (e), (f) show embeddings obtained using Euclidean distance and cosine similarity, respectively. Random initialization was used throughout, with a perplexity  $\mathcal{P} = 50$ .

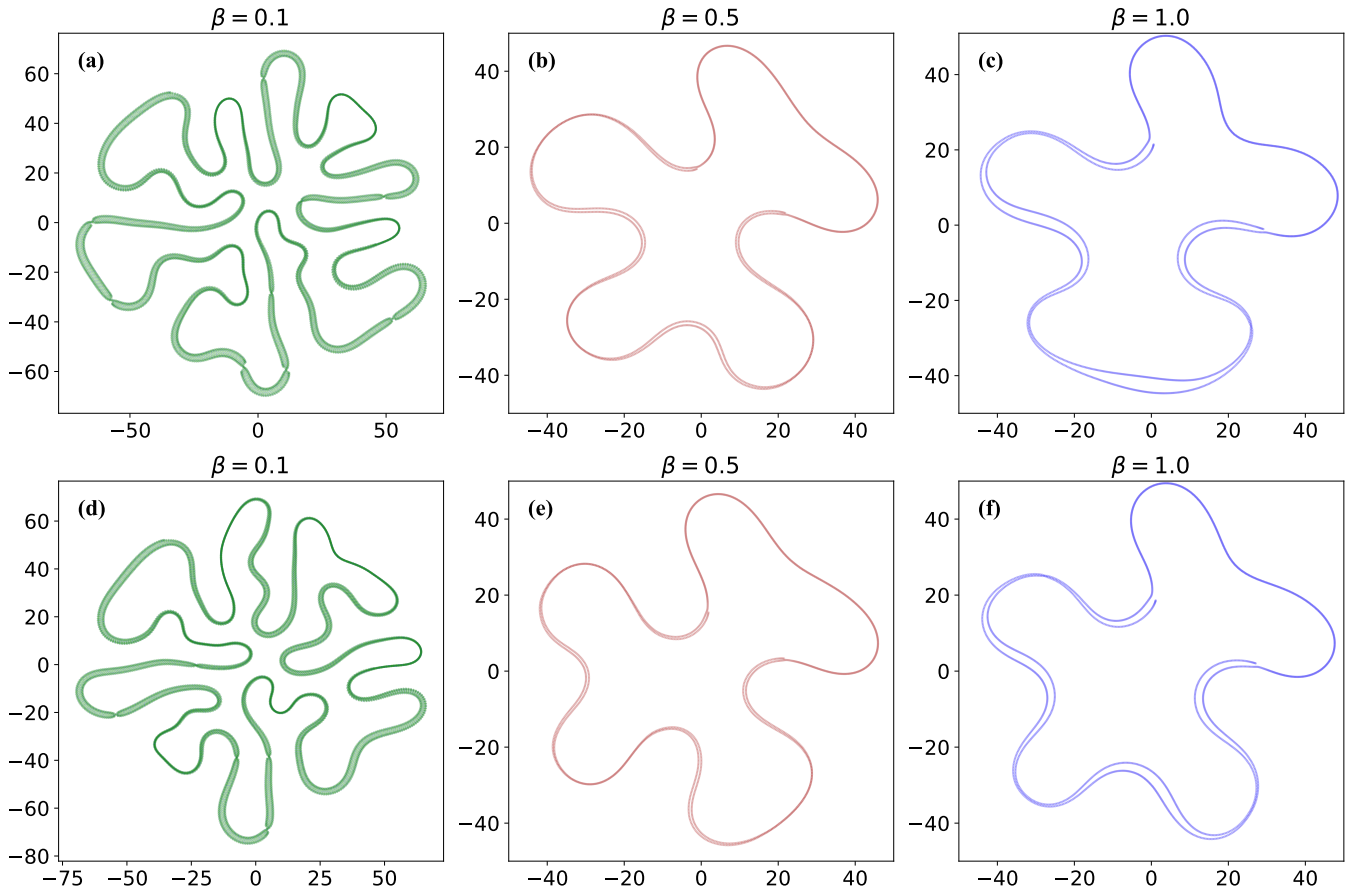


FIG. 18.  $t$ -SNE embeddings of the entire trajectories of early-stage dynamics, with  $n_s = 10,000$  and  $n_s = 2,000$  datapoints corresponding to  $\beta = 0.1$  and  $\beta = 0.5, 1$ , respectively. The top panels (a), (b), (c) and bottom panels (d), (e), (f) show embeddings obtained using Euclidean distance and cosine similarity, respectively. PCA initialization was used throughout, with a perplexity  $\mathcal{P} = 30$ .